Quality Assessment of Degraded Iris Images Acquired in the Visible Wavelength

Hugo Proença

Abstract—Data quality assessment is a key issue, in order to broad the applicability of iris biometrics to unconstrained imaging conditions. Previous research efforts sought to use visible wavelength (VW) light imagery to acquire data at significantly larger distances than usual and on moving subjects, which makes this *real world* data notoriously different from the acquired in the near infra-red (NIR) setup. Having empirically observed that published strategies to assess iris image quality do not handle the specificity of such data, this paper proposes a method to assess the quality of VW iris samples captured in unconstrained conditions, according to the factors that are known to determine the quality of iris biometric data: focus, motion, angle, occlusions, area, pupillary dilation and levels of iris pigmentation. The key insight is to use the output of the segmentation phase in each assessment, which permits to handle severely degraded samples that are likely to result of such imaging setup. Also, our experiments point that the given method improves the effectiveness of VW iris recognition, by avoiding that poor quality samples are considered in the recognition process.

Index Terms—Iris recognition, Visible-light iris images, Image quality assessment, Biometrics.

I. INTRODUCTION

Due to the effectiveness proven by the deployed iris recognition systems, the popularity of the *iris* biometric trait has considerably grown in the last few years. As an illustration, over 50% of the papers cited in a recent survey [5] were published since 2005. Several reasons justify this interest: (1) it is a naturally protected internal organ that is visible from the exterior; (2) it has near circular and planar shape that turns easier its segmentation and parameterization and (3) its texture has a predominantly randotypic chaotic appearance that is stable over lifetime.

Regardless a few recent innovations (e.g., the iris-on-the-move project [21]), deployed iris recognition systems are quite constrained: subjects may stop-and-stare close to the acquisition device while their eyes are illuminated by a near infra-red (NIR) light source that enables the acquisition of good quality images. Recently, several research initiatives sought to increase distance, relax acquisition constraints and make use of visible wavelength (VW) light imagery, which broads the applicability of this technology to forensic domains where the subjects cooperation is not expectable.

When compared to the traditional *NIR constrained* setup, the use of VW light and the uncontrolled lighting conditions engender notorious differences in the appearance of the

H. Proença is with the Department of Computer Science, IT - Instituto de Telecomunicações, SOCIA - Soft Computing and Image Analysis Group, University of Beira Interior, 6200-Covilhã, Portugal.
Manuscript received ? ?, ?; revised ? ?, ?.
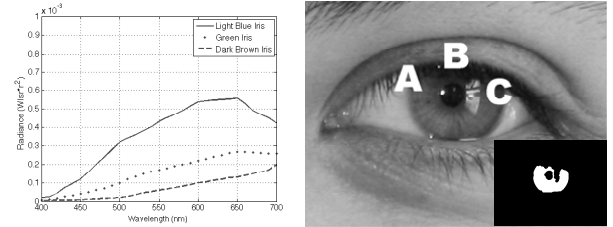
(a) Iris spectral radiance [14]   (b) VW iris image [32]

Fig. 1. The spectral radiance of the human iris in the VW highly varies according to the levels of iris pigmentation (figure a), which contributes for some of the noise factors (A,B,C of figure b) that degrade the quality of VW iris data. The bottom right corner plots the corresponding noise-free iris segmentation mask, obtained as described by He *et* al. [18].

captured data (figure 1). Acquiring images from significantly larger distances and on moving targets demands simultaneously high f-numbers and short exposure times for the optical system, in order to obtain acceptable depth-of-field values. These are in direct proportion to the amount of light required to proper imaging. The American and European standards councils ([2] and [7]) proposed safe irradiance limits for NIR illumination of near 10 mW / cm^2. In addition to other factors that determine imaging safety (blue light, non-reciprocity and wavelength dependence), these limits are a concern, as an excessively strong illumination can cause permanent eye damage. Moreover, the NIR wavelength is particularly hazardous, because the eye does not instinctively respond with its natural mechanisms (aversion, blinking and pupil contraction).

The pigmentation of the human iris consists mainly of two molecules: brown-black Eumelanin (over 90%) and yellow-reddish Pheomelanin [29]. Eumelanin has most of its radiative fluorescence under the VW, which enables to capture much more detail, but also more noisy artifacts (figure 1b). The feasibility of the *VW unconstrained* iris recognition remains controversial, specially for high pigmented irises that constitute the majority of the world's population, although preliminary experiments confirm the possibility of performing recognition in such challenging conditions [34].

As in many applications that deal with *real-world data*, segmentation is a major issue and has been motiving growing research efforts [35]: He *et* al. [18] used a clustering-based technique to roughly perform iris localization and an integro-differential constellation used for fine pupillary and scleric border detection, which not only accelerates the integro-

differential operator but also enhances its global convergence. Proença [33] considered the sclera the most easily distinguishable part of the eye and proposed a classification procedure based in the neural pattern recognition paradigm that runs in deterministic linear time, making the procedure suitable for real-time applications. As illustrated in figure 1b, these methods obtain acceptable results and effectively discriminate between the unoccluded regions of the iris (*noise-free*) and all the remaining data.

Subsequent to segmentation, quality assessment is a fundamental task. The goal is to quantify characteristics and fidelity of the segmented data, particularly in terms of its utility. This is essential, as performing recognition in too much degraded data decreases matching accuracy and increases computational complexity. This paper describes a method to assess the quality of VW iris images acquired in uncontrolled lighting conditions, at large (4 to 8 meters) distances and on moving subjects. When compared with previously published approaches, several discriminating factors can be pointed:

- The type of data that we aim to deal with. To the best of our knowledge, all the previously published methods were devised to NIR data acquired in constrained setups, while our proposal handles the specificities of *real-world VW* data.
- We empirically observed that published methods tend to fail in assessing the quality of VW data;
- We use the output of the segmentation stage in all quality assessments, which improves performance in some assessments (such as focus, described in section III-C) and makes others easier to assess (such as occlusions, described in section III-F).

The remainder of this paper is organized as follows: Section II summarizes the most recent proposals to assess iris image quality, grouping them according to various criteria. In Section III, we describe the proposed method in detail. Section IV reports the experiments and discusses our results. Finally, Section V concludes and points further work.

II. RELATED WORK

The concept of *good* metric is not trivial to determine, although the best one should maximally correlate with recognition effectiveness. Previous studies reported significant decays in effectiveness when data is degraded by each of the factors listed in Table I. Here, we overview the main techniques used to assess iris image quality with respect to each factor and compare them according to the used spectrum of light, the type of analyzed data (*raw* image, *segmented* or *normalized* iris region) and their output (*local* or *global*), as they operate at the pixel or image level. We note that most of the methods operate in NIR images and assess quality in the segmented data (either in the cartesian or polar coordinate systems). Exceptions are usually related with focus measurement, obtained by one of two approaches: (1) measuring the high frequency power in the 2D Fourier spectrum through a high-pass convolution kernel or wavelet-based decomposition ([10], [20] and [6]); (2) analyzing the sharpness of the iris borders through the magnitude of the first and second order derivatives ([1]

and [45]). Another key characteristic is the level of analysis: some methods operate globally (at the image level), usually to determine focus, gaze or motion blur ([20], [24] and [42]). As image quality varies across the iris, others operate at the pixel level to determine local obstructions ([1], [22] and [31]). Motion is estimated by detecting interlaced raster shear that might be due to significant movements during the acquisition of a frame ([11], [28], [43] and [49]). Other approaches rely in the response of the convolution between the image and directional filters, being observed that linear motion blurred images have higher central peak responses than sharp ones ([22] and [25]). Gaze is estimated by 3D projection techniques that maximize the response of the Daugman's integro-differential operator [22] and by the length of the axes of a bounding ellipse [49]. Eyelids are detected by means of line and parabolic Hough transforms [17], active contours [26] and machine learning frameworks [31] [44]. The modal analysis of the intensities histogram enables the detection of eyelashes [10] [17], as do spectral analysis [28] and edge-based methods [22]. As they usually are the brightest regions of images, specular reflections are detected by thresholds [22], while diffuse reflections are exclusive of VW data and more difficult to discriminate, being reported a method based in texture descriptors and machine learning techniques [31].

III. PROPOSED METHOD

A global perspective of the proposed method is given in figure 2. The input is a VW iris sample and its corresponding segmentation mask, obtained according to the method of [18]. The center of the iris (x_c, y_c) is roughly found and used to parameterize the deemed biologic pupillary and limbic iris boundaries ($\{x_{pi}, y_{pi}\}$ and $\{x_{si}, y_{si}\}$). These boundaries permit to assess the quality of severely degraded samples that will be extremely difficult to handle by traditional approaches. For comprehensibility, the generated quality scores are denoted everywhere by "α" and a subscript: α_f for focus, α_m for motion blur, α_a for off-angle, α_o for occlusions, α_p for iris pigmentation, α_c for pixel count (area) and α_d for pupillary dilation. As it is given in Table I, these quality factors are known to be strong correlated with recognition effectiveness and its assessment is made in a specific way for iris data. Other factors (such as Gaussian or salt and pepper noise) that are assessed in iris data as in any other type of images were not the scope of this work.

A. Estimation of the Iris Center

The convergence property of convex surfaces is the key insight this phase. The external boundary of the iris is predominantly convex, which was used to trace rays that pass through it and bend perpendicularly, converging into a *focal point* that gives an estimate of the iris center. As shown in figure 3, this gives a rough estimate of the true center, even in cases where the amount of unoccluded iris is very small. This approximation is acceptable because it is used as reference point by the shape descriptor that parameterizes the iris boundaries (normalized cumulative angular), which is

TABLE I
OVERVIEW OF THE MOST RELEVANT METHODS THAT WERE RECENTLY PUBLISHED AND ASSESS THE QUALITY OF IRIS BIOMETRIC DATA.

Method	Experiments Data Sets	Images	Analysis	Quality Assessment
Abhyankar and Schuckers[1]	CASIA.v3, BATH, WVU and Clarkson (NIR)	Segmented	Local, global	Occlusion (frequency analysis); focus (second order derivatives); contrast (hard threshold) and angular deformation (assigned manually)
Chen et al. [6]	CASIA.v3, WVU (NIR)	Segmented	Local, global	Focus and amount of information (2D isotropic Mexican hat wavelet-based frequency analysis)
Daugman and Downing[11]	ICE (NIR)	Raw data	Global	Effect of image compression; motion (interlaced raster shear)
Daugman [10]	ICE-1 (NIR)	Segmented	Local, global	Focus (magnitude of the response to a 5×5 high-pass kernel); off-angle (projective deformation that maximizes the circular shape of the pupil); eyelashes (intensities histogram modality)
Grabowski et al. [15]	-	Segmented and normalized	Global	Focus (entropy in the iris ring)
He et al. [17]	CASIA.v3 (NIR)	Segmented	Local	Eyelid (line Hough transform); eyelashes (intensities histogram modality)
Hollingsworth et al. [19]	Univ. Notre Dame (NIR)	Segmented	Global	Effect of pupil dilation
Jang et al. [20]	Yonsei (NIR, UBIRIS.v1 (VW)	Raw data	Global	Focus (ratio between the higher and lower frequency components, resultant of the dyadic discrete wavelet transform)
Kalka et al. [22]	CASIA.v3, WVU, ICE (NIR)	Segmented	Local, global	Focus (response to the Daugman's 8×8 high pass kernel); occlusion (morphologically dilated horizontal edges); motion blur (response to directional filters in Fourier space); off-angle (maximization of the circular integro-differential operator); specular reflection (threshold); lighting variation (intensities variance within small iris blocks); iris size (proportion of occluded pixels)
Kang and Park [23]	CASIA.v2(NIR)	Raw data	Global	Focus (magnitude of the response to a 5×5 high-pass kernel)
Kang and Park [24]	CASIA (NIR)	Segmented	Local	Eyelids (parabolic form fitting); focus (magnitude of the high frequency components; eyelashes (adaptive criteria according to the image blurring, convolution kernel for multiple eyelashes, first order differential for separable eyelashes)
Kang and Park [25]	CASIA.v3 (NIR)	Segmented	Local, global	Iris size; reflections (threshold); eyelids (parabolic form fitting scheme); eyelash (template matching based on continuity); motion blur (directional filters) and focus (frequency analysis)
Krishen et al. [26]	ICE (NIR)	Segmented and normalized	Local	Eyelids and eyelashes (gradient vector flow-based active contours method); focus (Gaussian mixture model learned from a set of image intensity histograms)
Nandakumar et al. [30]	WVU (NIR)	Segmented and normalized	Local, global	Focus and amount of information (2D isotropic Mexican hat wavelet-based frequency analysis)
Lu et al. [28]	CASIA.v3 (NIR)	Segmented and normalized	Local, global	Focus (energy of the frequency components resultant of a wavelet packet decomposition); motion blur (average difference of intensities between adjacent rows); eyelids (hard threshold) and eyelashes (frequency analysis in the upper and lower iris extremes)
Proença and Alexandre. [31]	UBIRIS.v1 (VW)	Segmented and normalized	Local	Glossy and specular reflections, eyelids and eyelashes (extraction of an 8D feature set, neural network classification scheme)
Wan et al. [42]	SJTU-IDB (NIR)	Raw data	Global	Focus (magnitude of the response to a 2D isotropic Laplacian of Gaussian kernel)
Wei et al. [43]	CASIA.v2 (NIR), UBIRIS.v1 (VW)	Raw data and segmented	Global	Focus (magnitude of high frequency components); motion blur (average difference of intensities between adjacent rows) and occlusions (thresholds)
Ye et al. [44]	CASIA, CASIA.v2 (NIR)	Raw data	Global	Iris occlusions and focus (pixels intensity feed neural network that detects the iris contour. A second network gives the data quality).
Zhang and Salganicoff [45]	-	Segmented	Global	Focus (sharpness of a portion of the pupillary border, based in the gradients' magnitude)
Zuo and Schmid [48]	CASIA.v2, WVU (NIR)	Segmented	Global	Pupil size (threshold); pupillary and scleric borders sharpness (cumulative gradient along the boundaries) and ROI homogeneity (difference between average intensities of the iris, pupil and sclera)
Zuo and Schmid [49]	ICE, MBGC (NIR)	Segmented	Local, Global	Interlacing (average difference between odd and even rows); illumination (average intensity of the segmented iris); lighting (intensity variance over small iris blocks); occlusions (proportion of occluded iris pixels); area (pixel count); pupil dilation (proportion between the iris and pupil); off-angle (ratio between the major and minor axis of a bounding ellipse) and blur (magnitude of the high frequency components)
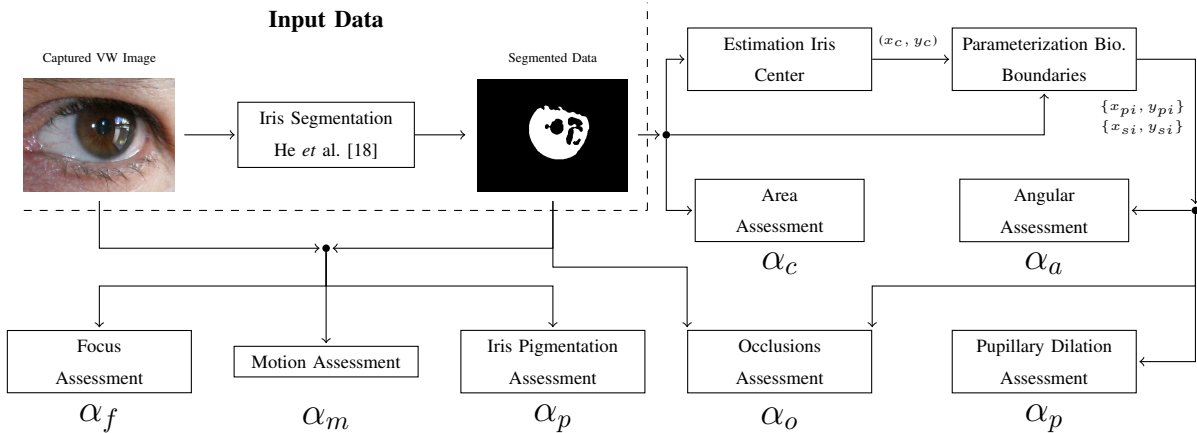
Fig. 2. Cohesive perspective of the proposed quality assessment method. The iris segmentation mask is used to roughly estimate the center of the iris. This value is used as reference point to reconstruct the deemed biological iris boundary and to assess each of the seven quality measures.

invariant to the reference point as long as it is inside the desired contour.

Let I be an iris image (h rows $\times$ w columns) and M the binary mask that gives the non-parameterized segmentation of its noise-free iris regions (bottom right corner of figure 1). Let $e = \{e_1, \ldots, e_n\}$ be the set of edge pixels of M, each e_i with coordinates (e_x, e_y). Let $\overrightarrow{v_i}$ be a vector tangent to the iris boundary at e_i and $\perp \overrightarrow{v_i}$ its perpendicular. A line l_i through point e_i and perpendicular to $\overrightarrow{v_i}$ is given by:

$$l_i = (b_x, b_y) + t \perp \overrightarrow{v_i} \qquad (1)$$

with $t \in \mathbb{R}$. Let $l = \{l_1, \ldots, l_n\}$ be the set of lines traced from e. We define an indicator function $\chi_1(x, y, l_i) \to \{0, 1\}$ that verifies wether the pixel (x, y) belongs to l_i:

$$\chi_1(x, y, l_i) = \begin{cases} 1, & \exists\, t \in]0, \sqrt{h^2 + w^2}] : (x,y) \in l_i \\ 0, & \text{otherwise} \end{cases}$$

The center of the iris (x_c, y_c) is estimated as the point where the maximal number of l_i intersect, i.e., where the accumulated value of χ is maximal.

$$(x_c, y_c) = \arg \max_{x,y} \sum_x \sum_y \sum_{i=0}^{n} \chi_1(x, y, l_i) \qquad (2)$$

where (x_c, y_c) give the coordinates of the iris center. Figure 3 gives two examples of this procedure: images in the left column have notoriously different proportion of noise-free iris and images in the right column give the accumulated $\chi_1(x, y, l_i)$ values. In both cases, the estimated center of the iris (denoted by the interception of the dashed lines) is acceptably close to the actual center.
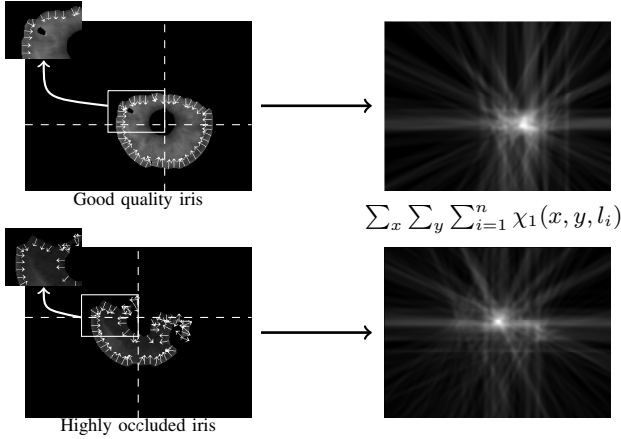
Fig. 3. Estimated iris center (interception of the dashed lines) in a relatively unoccluded iris (upper row) and a heavily occluded one (bottom row). Images of the right column give the accumulated $\chi_1(x, y, l_i)$ values.

B. Parameterization of the Biological Iris Boundaries

Efficient parameterization of the iris boundaries that are *behind* occlusions is a key issue regarding iris image quality assessment. Such boundaries not only permit to infer gaze, but also to estimate the proportion of occluded iris. This phase can be divided into two steps: (1) discriminate between the boundaries that correspond to iris biological borders and those that delimitate noisy regions; (2) reconstruct the biological iris boundary, according to the former boundary segments. The key insight is that biological boundaries can be faithfully described by periodic signals, which justifies the use of Fourier series for such purpose. Let (x_c, y_c) be the center of the iris and $f(x_c, y_c, \theta) = ((x_c - x_{\theta_j})^2 + (y_c - y_{\theta_j})^2)^{0.5}.M(x_{\theta_j}, y_{\theta_j})$ the Euclidean distance between (x_c, y_c) and the noise-free iris pixels in a given direction θ_j, where $(x_{\theta_j}, y_{\theta_j})$ are given by:

$$(x_{\theta_j}, y_{\theta_j}) = (x_c, y_c) + t \ [0, \ 1] \begin{bmatrix} cos(\theta_j) & -sin(\theta_j) \\ sin(\theta_j) & cos(\theta_j) \end{bmatrix}$$

with $t \in]0, \sqrt{h^2 + w^2}]$. Let $b^s = \{b_1^s, \ldots, b_n^s\}$ and $b^p = \{b_1^p, \ldots, b_n^p\}$, b_i with coordinates (x_i, y_i), be the noise-free iris pixels at respectively the farthest and closest distances from (x_c, y_c) in regularly spaced directions $\theta_i = \frac{2\pi i}{n}$, $i = 1, \ldots, n$.

$$(x_i^s, y_i^s) = \arg \max_{x_{\theta_i}, y_{\theta_i}} f(x_c, y_c, \theta_i), \ (x_i^p, y_i^p) = \arg \min_{x_{\theta_i}, y_{\theta_i}} f(x_c, y_c, \theta_i) \qquad (3)$$

b^s and b^p give the outer and inner iris boundaries, and the former is illustrated in figure 4a. Special attention should be paid to extremely occluded irises, where some of the b_i might not exist and should be discarded of further processing by a simple semantic rule. Next, the cumulative angular function [47] is used as shape descriptor of each type of boundary, defined as the amount of angular change from an arbitrary starting point:

$$\gamma(t) = \int_0^{\frac{Lt}{2\pi}} k(r) \ dr - k(0) + t \qquad (4)$$

where $t \in [0, 2\pi]$ and $k(r)$ describes changes in direction at point t with respect to changes in arc length L. Here, if the boundary is a perfect circle, the corresponding angular description $\gamma(t)$ will be 0, $\forall t \in [0, 2\pi]$. An illustration of the $\gamma(t)$ values is given in figure 4b. Segments of the boundary that correspond to biological borders are discriminated by statistical estimation of the $\gamma(t)$, $\frac{\partial \gamma(t)}{\partial t}$ and $\frac{\partial^2 \gamma(t)}{\partial t^2}$ values. As illustrated in figures 4b-4d, biological boundaries have evident smoother values and lower energy, which gives raise to different values of the objective function:

$$O(t) = \beta_0 \ \gamma(t) + \sum_{i=1}^{2} \beta_i \ \frac{\partial^i \gamma(t)}{\partial t^i} \qquad (5)$$

where β_i are regularization constants empirically obtained. Arguments of the first quartile of $O(t^*)$ — t^* regularly spaced in $[0, 2\pi]$ — are deemed to belong to the biological border and their coordinates (column and row) are illustrated by the dot and cross data points of figure 4e. The reconstruction of the complete biological border starts from these coordinates and is regarded as a nonlinear regression of a Fourier series of order r, given by:

$$c(x) = \frac{a_0}{2} + \sum_{k=1}^{r} (a_k \ cos(x\omega k) + a_{r+k} \ sin(x\omega k)) \qquad (6)$$

Constraining the fundamental frequency to $\omega = 1$ assures closure and completeness of the obtained contour. For each boundary, both the column and row coordinates are fitted similarly. Given a set of $t^*/4$ data points x_i, the goal is to optimize the parameter vector $\overrightarrow{a} = (a_1, \ \ldots, a_{2r+1})$ so as to minimize the sum of squares of the deviations:

$$S^2(\overrightarrow{a}) = \sum_{i=1}^{t^*/4} (y_i - c(x_i))^2 \qquad (7)$$

where y_i is the desired value at x_i and $c(x_i)$ the actual response. Requiring the zero-gradient condition to hold at the minimum:

$$\nabla S(\overrightarrow{a}) = J^T(y_i - c(x_i)) = 0 \qquad (8)$$

where J is the Jacobian. Let $b(\overrightarrow{a}) = -\nabla S(\overrightarrow{a}) = $

$-J^T(y_i - c(x_i))$, the zero gradient is given by $b(\overrightarrow{a}) = 0$, which is solved iteratively using the Newton-Raphson iterations and starting from an initial guess of $\overrightarrow{a}$, corrected to $\overrightarrow{a} + \Delta\overrightarrow{a}$. The increment $\Delta\overrightarrow{a}$ satisfies the linear equation $J^*(\overrightarrow{a}) \, \Delta\overrightarrow{a} = -b(\overrightarrow{a})$, where J^* is the Jacobian of b:

$$J^*_{ij} = \frac{\partial \, b_i}{\partial a_j} = \frac{-\partial^2 S}{\partial a_i \partial a_j} = -H_{ij} \tag{9}$$

As $J^* = -H$, $\Delta\overrightarrow{a}$ satisfies the system of linear equations:

$$H\Delta\overrightarrow{a} = b \tag{10}$$
$$\Delta\overrightarrow{a} = b \, H^{-1} \tag{11}$$
$$\Delta\overrightarrow{a} = H^{-1} \, J^T(y_i - c(x_i)) \tag{12}$$

Assuming moderate non-linearity, a reasonable approximation of H is given by $J^T J$, obtaining the next generation of the parameter vector $\overrightarrow{a}$. This is repeated until convergence is reached, i.e., $||\Delta\overrightarrow{a}|| < \alpha$, being α a very small positive value. An illustration of the reconstructed biological iris boundary is given in figure 4f.

C. Focus Assessment

As Table I summarizes, the Fourier domain is the most frequently used in focus assessment. The rationale is that focused data contains more high frequency components than blurred one. Daugman pointed out that defocus is equivalent to multiplying the 2D Fourier transform of a perfectly focused image by the 2D Fourier transform of a Gaussian kernel [9]. Thus, focus of an image I can be assessed by measuring its amount of high frequencies, i.e., the accumulated power of the convolution between I and a high-pass kernel H:

$$\alpha_f = \int_x \int_y |I * H|^2 dx dy \tag{13}$$

This measure performs well if images are dominated by the iris. Otherwise, if the iris is just a small part of the data — dominated by eyelashes or hair that are full of minutia — it tends to fail, which is particularly probable in uncontrolled image acquisition setups. Hence, focus is exclusively assessed in the region segmented as noise-free iris (using the segmentation mask M), avoiding the described problem. Also, assuming that segmentation inaccuracies predominate near the boundaries, we compared the results obtained when using exclusively the most interior regions of the noise-free irises (obtained by morphologic erosion of M and illustrated in the top images of figure 5), that have higher probability of actually being noise-free. Let M_p be an iris segmentation mask eroded by a circular structuring element of radius p. In order to keep the proportion of iris removed by erosion independent of the iris size, the radius of the structuring element is given by:

$$p = \arg\min_{p'} \sum_x \sum_y \frac{M_{p'}(x,y)}{M(x,y)} < T, \; p' = 1, \; \ldots, n \tag{14}$$

where T is an empirically adjusted threshold. In the experiments, we used a data set of 1 000 focused images

of the UBIRIS.v2 database D_1 and convolved them with Gaussian kernels $G(s,\sigma)$, $(s,\sigma) = (5i, 2i)$, $i = 2, \ldots, 4$, obtaining three increasingly defocused versions of the data set: $\{D_2, D_3, D_4\}$. As it is given in the bottom row of figure 5, we compared the α_f values obtained by the Daugman [9] and Kang and Park [23] kernels when using: (1) the whole image; (2) the whole iris and (3) the most interior iris regions as input data. The plot at the bottom left corner gives the proportion between the average α_f values of consecutive data sets, i.e., $\sum_2^4 \overline{d_{i-1}}/\overline{d_i}$, where $\overline{d_i} = \frac{1}{n} \sum \alpha_f(i)$ is the average focus value in the D_i data set. Maximal separation was obtained around $T = 0.4$ (Daugman kernel) and $T = 0.3$ (Kang and Park kernel), which is justified by the smaller size of the latter kernel. Plots at the center and right contextualize the results, comparing the $\overline{d_i}$ values obtained when using the whole image (dashed lines), the whole iris (continuous lines) and the interior iris regions (with $T = 0.35$, dotted lines) as source data. It can be confirmed that both spectral measures perform acceptably in VW data and that results were consistently improved when exclusively the most interior iris regions were used as input (defocused versions of D_i obtained the lowest focus scores).

D. Motion Assessment

There are various causes for motion blurred iris images, corresponding to the different types of movements in the scene: subjects, heads, eyes and eyelids, causing motion to be non-linear and particularly hard to determine and compensate for. In previous works, an oversimplification was made and assumed that motion is linear across the image, which cannot be guaranteed in unconstrained acquisition setups. Instead, we exclusively assumed that motion is linear in the iris ring and concerned about the detection of linear motion blur inside an iris bounding rectangle $B(x,y)$. The rationale is that linearly motion-blurred data has frequency responses with visible parallel strips of direction θ that correspond to the motion direction. As suggested by Kalka et al. [22], the width and power of these strips provide an estimate of the amount of motion. We used the concept of power cepstrum $C(B) = |F(log(|F(B(x,y))|))|^2$, illustrated in three images of figure 6: a sharp and two motion-blurred. The primary direction of motion is deemed to be the one that minimizes the power of the derivatives of $C(B)$ along a direction $\theta_i \in [0, 2\pi]$.

$$\theta_m = \arg\min_{\theta_i} G(\sigma, r) * \sum_x \sum_y \left(\frac{\partial}{\partial\theta_i} C(x,y)\right)^2 \tag{15}$$

$\frac{\partial}{\partial\theta_i} C(x,y)$ gives the partial directional derivative of C along the θ_i direction ($\theta \in [0,\pi]$), obtained as described in [39]. The amplitude α_m of the partial directional derivatives in $[0, 2\pi]$ gives the motion quality score, as illustrated in figure 6d:

$$\alpha_m = \max_{\theta_i} \sum_x \sum_y \left(\frac{\partial}{\partial\theta_i} C(x,y)\right)^2 - \min_{\theta_i} \sum_x \sum_y \left(\frac{\partial}{\partial\theta_i} C(x,y)\right)^2 \tag{16}$$

(a) b^s

(b) $\gamma(t^*)$

(c) $\frac{\partial \gamma(t)}{\partial t} * G(\sigma, r)$

(d) $\frac{\partial^2 \gamma(t)}{\partial t^2} * G(\sigma, r)$

(e) Fourier regression

(f) Reconstructed boundary
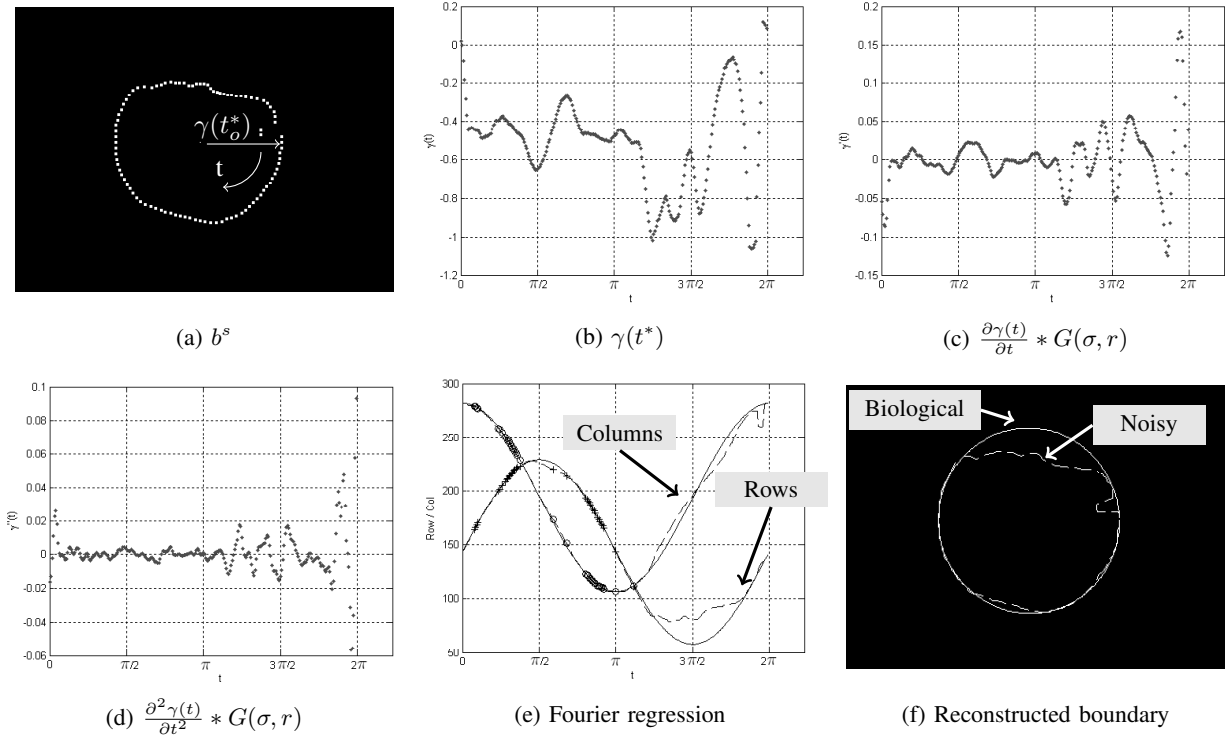
Fig. 4. Estimation of the biological scleric border. The boundary points that are farthest from the iris center at each direction (figure a) are used to obtain the cumulative angular description $\gamma(t^*)$ of the contour (figure b) and its first and second order derivatives (figures c and d). The selection of the regions deemed to belong to the iris biological boundary (cross and circular data points of figure e) enables the reconstruction of the deemed biological border through a regression of a Fourier series (figure f).
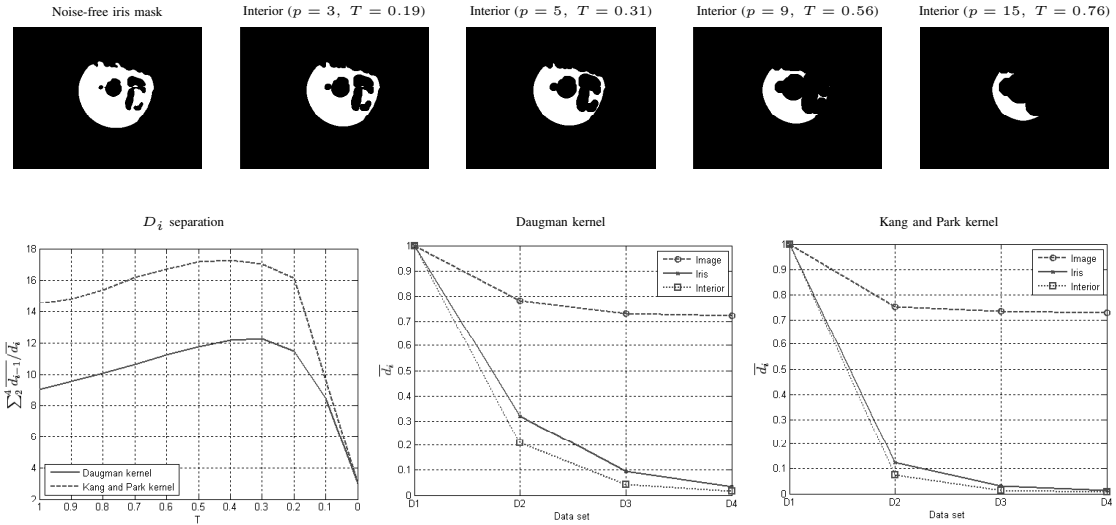
Fig. 5. The upper row shows an iris mask and its increasingly most interior iris regions. The bottom left figure shows the separation between the focus scores obtained in defocused versions of the training data set, in respect to different values of T. The bottom center and right plots illustrate the improvement observed when just the most interior iris regions are used as source data (dotted lines), instead of the whole image (dashed lines) or whole iris (continuous lines).

E. Off-Angle Assessment

Assuming the circularity of the pupil as a measure of the off-angle, Kalka *et* al. [22] and Dorairaj *et* al. [13] projected an integro-differential operator at multiple yaw and pitch angles, yielding an optimization process in a 5D hyperspace with

significant computational efforts. Daugman [10] used Fourier series expansions of the 2D coordinates of the pupillary boundary, which contain shape distortion information that is related to deviated gaze. Expressing the pupillary boundary as a set of coordinate vectors $X(t)$ and $Y(t)$, the direction and magnitude

(a) No motion

(b) Blurred, $(\theta, \alpha) = (\frac{\pi}{2}, 0.22)$

(c) Blurred, $(\theta, \alpha) = (\frac{\pi}{4}, 0.21)$

(d) Directional derivatives
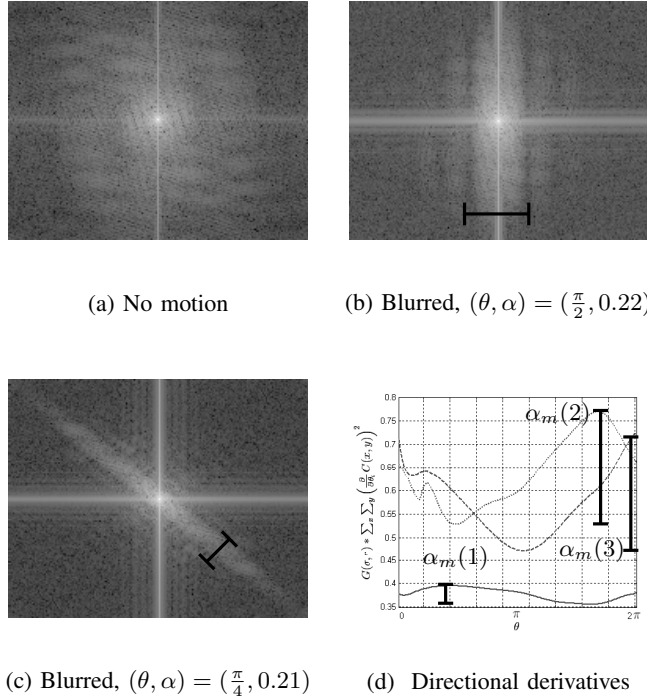
Fig. 6. Power cepstrum of a sharp iris (figure a) and of two motion blurred irises (figures b and c). Figure d gives the accumulated image derivatives along θ directions, where the minimum values indicate the primary blur direction. The amplitude of this signal is also used to discriminate between motion blurred and sharp irises, as $\alpha_m(2), \alpha_m(3) \gg \alpha_m(1)$.

of the gaze deviation are contained in the form of Fourier coefficients on the harmonic functions cos(t) and sin(t) that — linearly combined — represent $X(t)$ and $Y(t)$. Algebraic manipulation estimates from four Fourier coefficients two gaze deviation parameters θ and γ. Our aim is to obtain a unique value that gives the magnitude of the deviation (used as quality score) and other one that corresponds to its major direction. The rationale is that the degree of circularity of the scleric boundary should be inversely correlated to off-angle acquisition. For such, we used the concept of minimal bounding rectangle and compared the length of its sides. Let $b^* = \{b_1^*, \ldots, b_n^*\}$ be the coordinates of the biological scleric boundary, that delimitates a convex polygon P. As proposed in [16], (x_m, x_M, y_m, y_M) are the coordinates of the four extreme points of P, where m and M stand for the minimum and maximum values. Let $l_j : 1 \leq j \leq 4$, be four line segments through the extreme points and θ the minimal rotation such that one l_j coincides with a line segment defined by (b_i^*, b_{i+1}^*). Let $l_j^\theta : 1 \leq j \leq 4$ be the versions of l_j rotated by θ. Minimizing the area of the enclosing rectangle is equivalent to keep the minimum of successive rotations, until the lines have been rotated by an angle greater than 90 degrees. Let $l_j^* : 1 \leq j \leq 4$ be the line segments that delimitate the minimum enclosing rectangle of extreme points $(x_j, y_j) : 1 \leq j \leq 4$. Let d_M and d_m be the lengths of these line segments, such that $d_m \leq d_M$. The magnitude of the deviation $\alpha_a : \mathbb{R}^{n \times 2} \to]0, 1]$ and its major direction $\theta_a : \mathbb{R}^{n \times 2} \to [-\pi, \pi]$ are obtained as follows:

$$(\alpha_a, \theta_a) = \left(1 - \frac{d_m}{d_M}, \arctan(\overrightarrow{v})\right) \qquad (17)$$

where $\overrightarrow{v} = \frac{(x_i, y_i) - (x_j, y_j)}{d_M}$, such that $y(j) \leq y(i)$ and $((x_i - x_j)^2 + (y_i - y_j)^2)^{0.5} = d_M$. Figure 7 illustrates three iris images and the corresponding off-angle scores: image in the left column was frontally captured and the others resulted of moderated (central column) and severe deviations (right column) in image acquisition.

F. Occlusions Assessment

An estimate of the amount of iris that is occluded by other types of data is obtained by comparing the area inside the deemed biologic iris ring (inside the scleric $\{s_1^*, \ldots, s_n^*\}$ and outside the pupillary contour $\{p_1^*, \ldots, p_m^*\}$), and the area of the noise-free iris segmentation mask. Assuming the convexity of the polygon defined by the set of vertices $\{b_1^*, \ldots, b_n^*\}$, a pixel is on the interior of this shape if it is always on the same side of all line segments defined by (b_i^*, b_{i+1}^*), $b_i^* = (x_i, y_i)$. Let $z_i = f(x, y, b_i^*, b_{i+1}^*) : \mathbb{N}^6 \to \mathbb{R}$, be a function that relates the position of (x, y) to the straight line defined by $z_i = (y - y_i)(x_{i+1} - x_i) - (x - x_i)(y_{i+1} - y_i)$.

An indicator function that discriminates between pixels inside and outside the iris ring is given by:

$$\chi_2(x, y) = \begin{cases} 1 & , \text{if } \forall j, j' : z_j^s . z_{j'}^s > 0 \wedge \exists k, k' : z_k^p . z_{k'}^p < 0 \\ 0 & , \text{otherwise} \end{cases}$$
$$(18)$$

where $j, j' \in \{1, \ldots, n\}$ and $k, k' \in \{1, \ldots, m\}$. Function $o : \mathbb{N}^{w \times h} \times \mathbb{N}^{w \times h} \to [0, 1]$ has direct correspondence to the proportion of iris occluded by noise:

$$\alpha_o(I, M) = \frac{1}{n} \sum_x \sum_y \left(\chi_2(x, y) - \left(\chi_2(x, y) \, M(x, y)\right)\right)$$
$$(19)$$

where n is the area of the iris ring. Figure 8 gives some examples of this procedure: white pixels denote regions segmented as noise-free that are inside the deemed biological boundaries; dark and light gray regions respectively denote occluded iris pixels and regions outside the deemed biological boundaries. It can be confirmed that assessments match the intuitive human perception, either for almost unoccluded, moderately or severely occluded iris images.

G. Levels of Iris Pigmentation

The spectral radiance of the iris in respect of its level of pigmentation has greater variance in the VW than in the NIR, which increases the heterogeneity of the captured data: light pigmented irises provide more detail than heavy pigmented, although the number of visible crypts, arching ligaments, freckles and contraction furrows significantly varies between subjects. Also, the appearance of the striated anterior layer that covers the trabecular meshwork depends of the amount of light used in the acquisition process. Here, we propose a strategy to assess the levels of iris pigmentation based in the observation that local *hue* and *value* across the iris vary

$$(\alpha_a, \theta_a) = (0.02, 2.52) \qquad (\alpha_a, \theta_a) = (0.13, 0.29) \qquad (\alpha_a, \theta_a) = (0.20, 1.43)$$
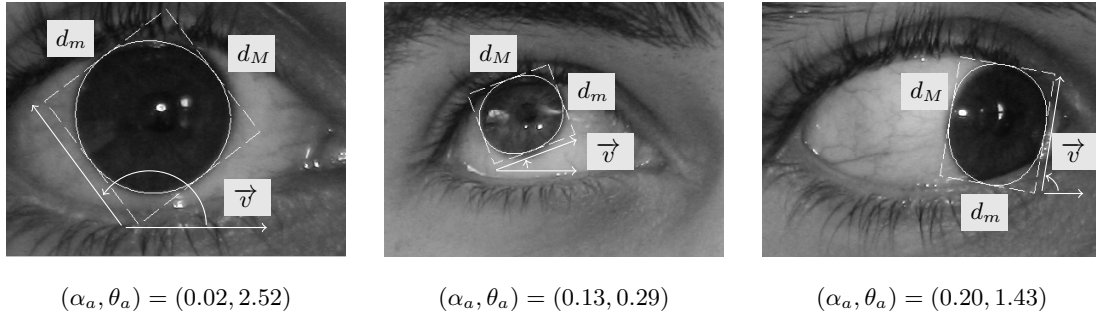
Fig. 7. Examples of the proposed off-angle assessment, for aligned, moderately and severely deviated iris images.

$$\alpha_o = 0.032 \qquad \alpha_o = 0.178 \qquad \alpha_o = 0.345 \qquad \alpha_o = 0.485$$
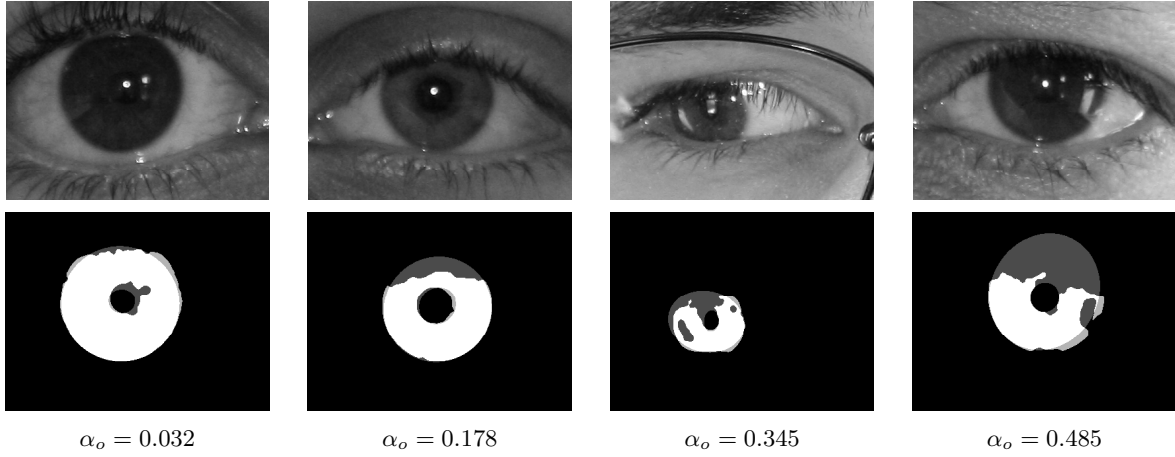
Fig. 8. Examples of the proposed iris occlusions assessment, for practically unoccluded, moderately and severely occluded iris images. White regions were segmented as noise-free and are inside the deemed biological boundaries. Dark and light gray regions respectively denote noisy iris pixels and regions outside the biological boundaries.

accordingly to its levels of pigmentation. Also, we consider the average brightness of a region deemed to contain the sclera, adjusting for different lighting conditions. Let I_{hsv} be the iris image represented in the HSV color space. Let $\{e_1, \ldots, e_n\}$ be the set of edge pixels of M that are farthest from (x_c, y_c) in n regularly spaced directions ($n \in [0, 2\pi]$). Let $d = \{d_1, \ldots, d_w\} : w = \sum_{i=1}^{n-1} i$, be the Euclidean distances between elements of e. The third quartile of d corresponds to the farthest distances between edges, which associated vectors tend to point to the direction of the sclera (avoiding eyelids and eyelashes occlusions). The direction of the sclera is given by the mean direction of the vectors drawn from these farthest points, i.e., $\overrightarrow{v} = \frac{4}{w} \sum_{i=1}^{w/4} (x_i - x_j, y_i - y_y)$. Thus, $(x_c, y_c) \pm k \overrightarrow{v}$ delimitate an image strip that spreads in direction $\overrightarrow{v}$ and is illustrated in the left column of figure 9. Let B be a binary mask, such that $B(x, y) = 1$ inside the band and 0 otherwise. The levels of iris pigmentation are obtained by relating the hue and value of the iris and of the sclera pixels inside this band:

$$\alpha_p(I) = \frac{m_1 \sum_x \sum_y \left(I_{hv}(x,y) \ M(x,y) \ B(x,y) \right)}{\beta \ m_2 \ \sum_x \sum_y \left(I_{hv}(x,y) \ B(x,y) \ (1 - M(x,y)) \right)} \tag{20}$$

where $m_1 = \sum\sum B(x,y)(1 - M(x,y))$ and $m_2 = \sum\sum B(x,y)(M(x,y))$. $I_{hv}()$ gives the pixel *hue* and *value* and $\beta \in [0, 1]$ is a regularization term. According to a set of manually classified 300 iris images of *light* and *heavy* pigmented irises, a k nearest neighbors strategy classifies the sample into one of k classes w_i: $w_i = k_l/(k_l + k_w)$, where k_l and k_h represent the number of light and heavy pigmented irises in the nearest neighbors. The plot at the right of figure 9 gives the α_p values of the training set, where circular and cross data points represent light and heavily pigmented irises.

H. Pixel Count, Pupillary Dilation and Amount of Information

Three other factors that are known to play relevant roles in the recognition effectiveness are discussed in this section: the area of the noise-free data, the pupillary dilation and the amount of information within the iris, which were grouped in a single section due to the simple way they are obtained. The area of the non-occluded iris region is simply given by the number of pixels classified as noise-free by the segmentation algorithm, i.e., $\alpha_c = \sum_x \sum_y M(x, y)$. An assessment of the pupillary dilation α_d is given by the ratio between the area of the polygons defined by the scleric and pupillary biological boundaries, both estimated in section III-B. Finally, an estimate of the the amount of information can be given

B image strips   Training set feature values
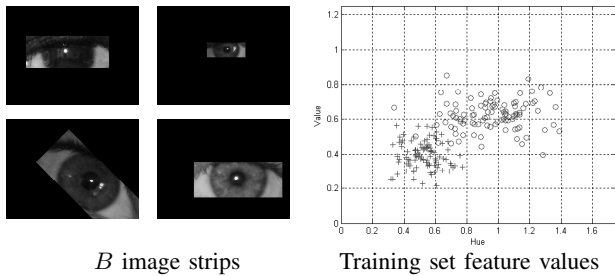
Fig. 9. Images at the right column illustrate the image band deemed to contain the sclera. Plot at the center gives the α_p values of a training set of 300 images, where circular and cross points represent light and heavy pigmented irises.

by the local entropy values in small windows of the iris ring. However, we decided not to use it as quality score, since we observed that this value is heavily correlated with the focus score and relatively invariant to other parameters (such as acquisition distance and levels of iris pigmentation).

I. Temporal Computational Complexity

The computational complexity of the given method was a major issue, in order to handle real-time data. Here we analyze the complexity of each phase and give statistics about its execution time. It should be noted that values should be regarded as upper bounds, as they were obtained using an interpreted language and without any performance optimization concerns. Let I be an RGB image with $n = c \times r$ pixels and M be its corresponding binary segmentation mask (in our experiments $120\ 000 = 400 \times 300$). Although this is a relatively large value, the phases with highest computational complexity depend of the number of edge pixels n_e of M in θ directions ($n_e \ll n$, between 64 and 512 in our experiments). As these are relatively low values, the increased computational complexity is not a concern and does not significantly affect performance.

The estimation of the center of the iris (an evidence-gathering process) has time complexity of $O(n_e^2)$. The parameterization of the iris boundaries receives $2 \times n_e$ values, described by means of the cumulative angular descriptor ($O(n_e^2)$) and used in a nonlinear regression of a Fourier series with time complexity bounded by $O(\log(n_e)\ n_e)$. Focus is assessed by the convolution between the noise-free iris pixels n_f ($n_f \ll n$) and a high pass kernel, which can be done in quadratic time with respect to n_f ($O(n_f^2)$). Motion was assessed by means of the power cepstrum of the n_b pixels within an iris bounding box ($\overline{n_b} \simeq \frac{n}{8}$), having time complexity ($O(n_b^2)$) . Off-angle assessment uses the concept of minimal bounding rectangle and of its minor and major axis, which runs in time deterministic linear to its input ($O(n_b)$). Occlusions are assessed by measuring the proportion between two areas: one given by a point-in-polygon algorithm (linear complexity) and the other composed by the n_f iris pixels ($O(n_f^2)$). Finally, the levels of iris pigmentation are estimated by the average hue and value in an image band, with respect to a data training set, which is done in $O(n_b^2)$. In our earliest experiments we

used a lazy classification algorithm (nearest neighbors), and then explicitly defined the decision boundaries, which has significantly improved performance.

Experiments were performed in a 2.66 GHz iMac with 8GB 1067 MHz DDR3 memory, using an interpreted programming language and without any performance optimization concerns. Even so, the observed average execution time for the complete assessment was $0.68s. \pm 0.22$ for 200×150, $1.36s. \pm 0.45$ for 400×300 and $2.74s. \pm 0.91$ for 800×600 images (95% confidence intervals). These values led us to conclude that, if appropriate programming languages and hardware are used, performance should easily be improved by two orders of magnitude and real-time performance achieved.

IV. EXPERIMENTS

This section describes our experiments during the evaluation of the proposed method. Several examples are illustrated and discussed, the used data sets described and the improvements in recognition effectiveness highlighted. Finally, we discuss the adaptability of the proposed method to NIR data.

A. Results and Discussion

For the purpose of contextualization, our method was evaluated in two dramatically different VW iris data sets: UBIRIS [32] and UPOL [40]. The former fits better the scope of this work and was used as main experimental data source. Its images were captured from moving subjects, at varying distances (4 to 8 meters) and in uncontrolled lighting conditions, resulting in extremely heterogeneous images with several factors that degrade their quality. Oppositely, UPOL images were acquired with an optometric framework and according to a rigid protocol, which resulted in almost noise-free images.

In order to avoid that segmentation errors corrupt the results, a subset of 10 427 images was selected, which under visual inspection we verified that the method of He *el* al. [18] has accurately segmented. We performed quality assessment in this set, obtaining the histograms given in figure 10. In order to better match the human perception of *quality*, scores were grouped according to their numeric range. Each group is shown as one bin labeled in the $[1, 10]$ discrete range, regarded as a quantized and normalized quality score. For comprehensibility, normalized scores are denoted by α^* plus the same subscripts as before. The horizontal range of the leftmost and rightmost bins extends to include the entire data range. For focus, motion, off-angle, occlusions, iris area and pupillary dilation plots, *better* quality values are given in the rightmost bars (in the pigmentation plot rightmost bars denote the lightest pigmented irises). It can be seen that the large majority of images were classified as focused and without significant motion-blur. We observed that over $\frac{1}{3}$ of them are off-angle and about $\frac{1}{2}$ have moderated to severe iris occlusions. Most of the subjects (caucasian latin) have dark and medium dark irises that were captured from varying distances, which resulted in irises of very different sizes. These results appear to be in agreement to the acquisition protocol of the data set [32],

(a) *Focus*   (b) *Motion*   (c) *Off-angle*

(d) *Occlusions*   (e) *Iris Pigmentation*   (f) *Iris Area*   (g) *Pupillary Dilation*
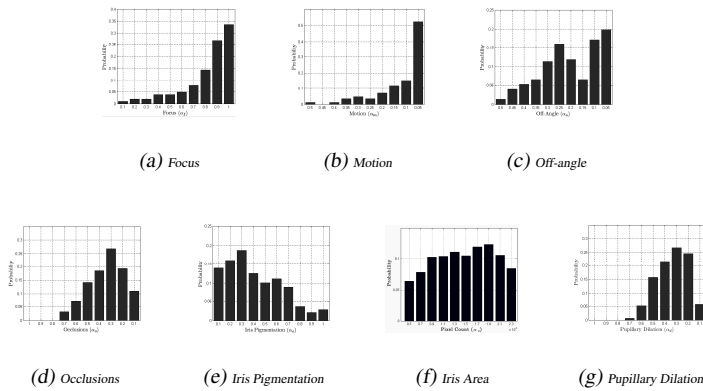
Fig. 10. Quality assessments obtained for the UBIRIS.v2 database. For all plots, *better* quality are expressed by rightmost bars. For the iris pigmentation plot, light pigmented irises are represented by rightmost bars.

which we consider a good metric for the effectiveness of the proposed quality assessment.

Figure 11 gives several examples of our quality assessments, being shown the original quality score α and the corresponding quantized and normalized value α^* between parenthesis (according to the previously found horizontal range values) [1]. The example given in the first column and left row ($\{1,1\}$) is an image of relative good quality, from where 128 points deemed to belong to the biological boundary were extracted. These came mostly from the inferior parts of the iris due to minor occlusions in its upper region, which justifies the good α_o score (9 in 10). Image was classified as focused and the iris as light pigmented, which matches the human perception. Examples given in positions $\{1,2\}$ and $\{2,2\}$ illustrate two severely degraded samples, from where the biological borders were correctly estimated. In both cases the selected points came from the nasal and temporal boundaries of the iris, which are known to have smaller probabilities of being occluded. From our viewpoint, these are good examples of the effectiveness of the proposed strategy in dealing with severely degraded data. Image at position $\{3,1\}$ is from the UPOL database and is noise-free, which has evident correspondence in the almost maximal normalized quality scores. Finally, figure in $\{3,2\}$ illustrates a failure case due to problems in discriminating between the biological and noisy boundaries. This occurs mostly when the noisy boundaries are very smooth and deemed as biological by the objective function (5). We hope that a set of semantic rules avoids this problem.

B. Improvements in Recognition Effectiveness

In evaluating the improvements in recognition effectiveness achieved due to quality assessment, we used the classical Daugman's recognition strategy [10], as it is the unique that is actually functioning in commercially deployed systems and is clearly the most well known. According to this choice, the segmented boundaries were normalized to dimensionless polar coordinates. Then, a bank of Gabor filters was used

[1]More examples can be found at http://www.di.ubi.pt/~hugomcp/doc/examplesVWIQ.htm

to analyze the iris texture and the angle of each phasor quantized to one of four quadrants. Finally, the fractional Hamming distance gave the dissimilarity between two irises. As suggested by Daugman [8], for two-choice decisions (e.g., match/non-match) the decidability index d' measures how well separated are the two types of distributions and recognition errors correspond to their overlap area. It is given by:

$$d' = \frac{|\mu_E - \mu_I|}{\sqrt{\frac{1}{2}(\sigma_I^2 + \sigma_E^2)}} \qquad (21)$$

where μ_I and μ_E are the means of the two distributions and σ_I and σ_E their standard deviations.

Our tests were performed in an "one-against-all" comparison scheme. Figure 12 compares the histograms of the fractional Hamming distances obtained for the match (light bars) and non-match (dark bars) comparisons without quality assessment (figure 12a) and when the quality scores are used to reject samples with $q = min\{\alpha_f^*, \alpha_m^*, \alpha_c^*, \alpha_d^*, \alpha_p^*, \alpha_o^*, \alpha_a^*\}$ below 5 (figure 12b) and 7 (figure 12c). The line plots correspond to the fitted Normal distributions and the upper left corner gives the corresponding decidability index d'. As general considerations, we observed that values obtained for the non-match distributions were similar to values reported for the NIR setup, which points that the probability for a false acceptance is independent of data quality. Oppositely, there is a significant movement of the match distributions toward the non-matches, substantially increasing the probability for false rejections if traditional acceptance thresholds are used. Due to this, the decidability of the VW recognition systems is much lower than the corresponding value reported for the NIR setup.

Interestingly, the observed primary effect of quality assessment was to counterbalance the above referred movement, as illustrated in figures 12b and 12c. It can be seen that match distributions tend to become narrower and slight to the right when samples with quality $q < 5$ and $q < 7$ were not used in the recognition tests. This is reiterated in figure 12d that compares the match (dashed lines) and non-match (continuos lines) distributions according to the minimum value of q. We concluded that quality assessment improves recognition effectiveness by consistently shifting the histogram of the match comparisons to the left, which improves the decidability of the resulting PR systems and is of specially interest for noisy acquisition environments, where both types of distributions largely overlap. Moreover, the amplitude of such match movement appears to be in direct proportion to the minimal quality of samples.

Figure 13a shows how the true and false matches in our system would change according to different decision thresholds, when no quality is considered (continuous line) and when only samples with $q \geq 5$ (dash-dotted line) and $q \geq 7$ (dashed line) are considered for recognition. Here, we plot the area under curve (AUC) for all three setups, which significantly augments as the poorest quality samples are rejected. Figure 13b shows how the decidability values d' vary with respect to the minimum value of q. The gray regions denote confidence intervals of 95%. Again, we confirmed that samples with poor quality considerably shift the histogram of
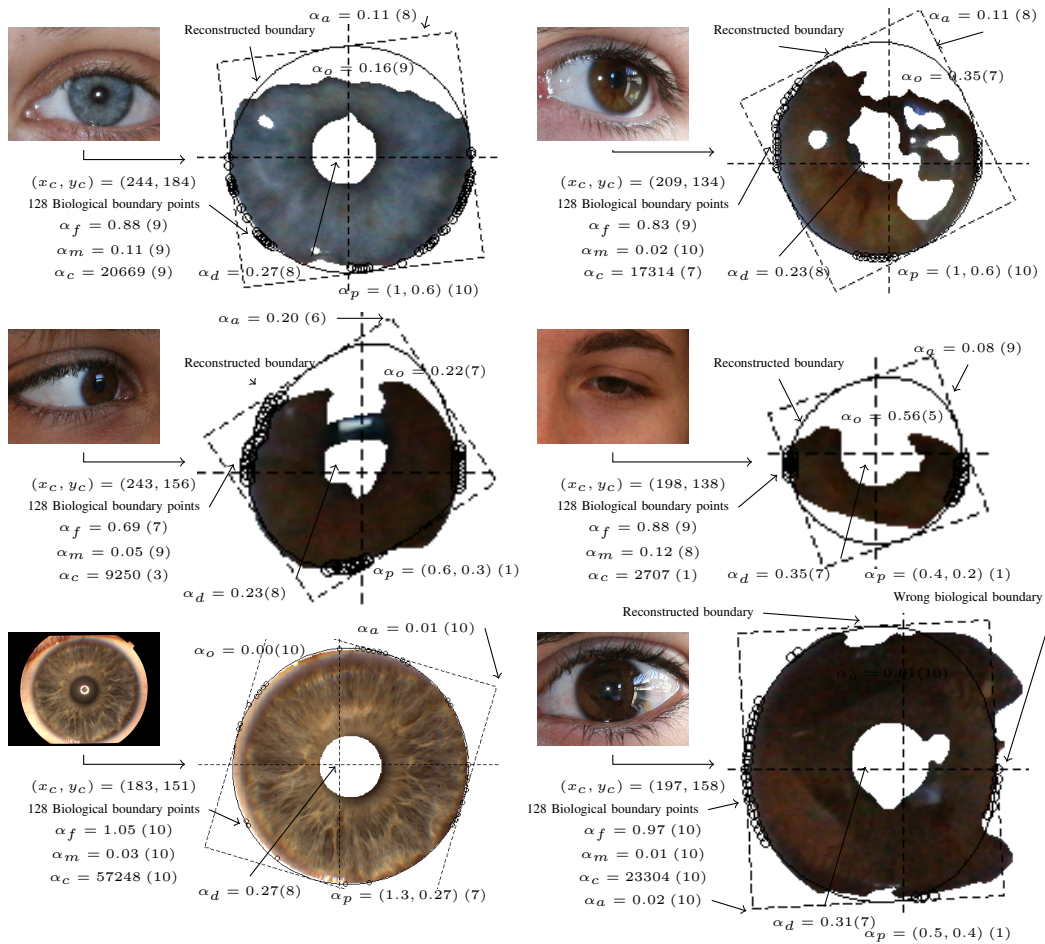
Fig. 11. Examples of the proposed quality assessments. Seven quality scores are given (focus, motion, off-angle, occlusions, pigmentation, pixel count and pupillary dilation), along with the corresponding quantized and normalized scores between parenthesis. For the focus, motion, off/angle, occlusions, iris area and pupillary dilation scores *better* values correspond to higher scores. For the pigmentation scores, higher values correspond to the lightest pigmented irises.

the match distributions toward the non-matches, and consistently reduce the separability between both distributions. We know of two possible explanations for the sigmoid appearance of the decidability curve: (1) for some of the noise factors (e.g., blur) it appears that just heavily degraded data degrades performance and (2) the excessive number of beans used in score quantization leads that data of adjacent normalized scores has actually very similar quality that, even for humans, is very difficult to discriminate.

C. Analysis of Individual Factors

The next question to consider is about the effect of each quality score in recognition effectiveness. For such, we repeated the "one-against-all" recognition setup, but selecting exclusively samples with minimal quality according to each type of score. Figure 14 gives the obtained decidability values with respect to the quantized quality scores α^* in each type of assessment ($\alpha^* \in [1, 10]$ as in the previous experiments). Again, rightmost regions correspond to data with better quality and the gray regions denote 95% confidence intervals. It should be noted that although this experiment enables to perceive *how much* recognition effectiveness is degraded by

each type of quality score, it cannot be regarded as an effective evaluation. This will demand a data set with images degraded exclusively by one factor and UBIRIS.v2 images (as well all the remaining available data sets) are simultaneously degraded by various factors.

Even so, several degradation patterns are evident and able to be discussed. At first, the major effect that gaze deviations have in recognition effectiveness (figure 14b), when compared to other factors. We suspect that such perspective deformations cause significant changes in phase, which significantly perturb the used feature extraction and matching strategies. We also confirmed the minor impact of focus in recognition effectiveness (figure 14a), as it is known that most of the iris discriminating information spans between 2 and 3 octaves of the original scale and only severe defocus would notoriously affect the recognition process. In our opinion this is one of the biggest advantages of the iris, when compared to other biometric traits: using the lowest and middle-low frequency components for recognition improves the robustness to noise (focus and artifacts).

Our observations about the degradation in effectiveness due to pupillary dilations were inconclusive, in opposition with

(a) Fractional Hamming distances without data quality assessment.

(b) Fractional Hamming distances between samples with minimal quantized quality above 5 ($q \geq 5$).

(c) Fractional Hamming distances between samples with minimal quantized quality q above 7 ($q \geq 7$).

(d) Fractional Hamming distances with respect to the minimal quality of samples (q).
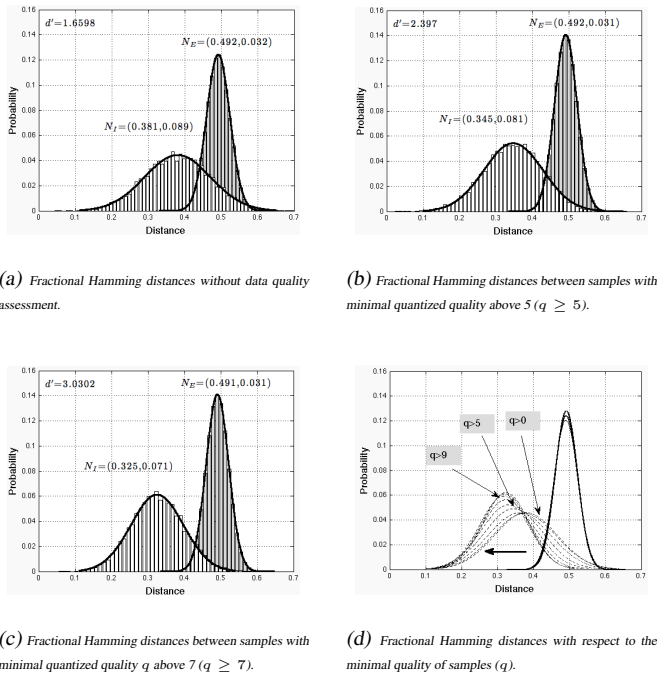
Fig. 12. Comparison between the distributions of the fractional Hamming distances for match (white bars) and non-match (gray bars) distributions, according to the minimum quality of samples q.

(a) ROC curves corresponding to the distributions illustrated in figure 12.

(b) Variation in the PR decidability index d' according to the minimal image quality.
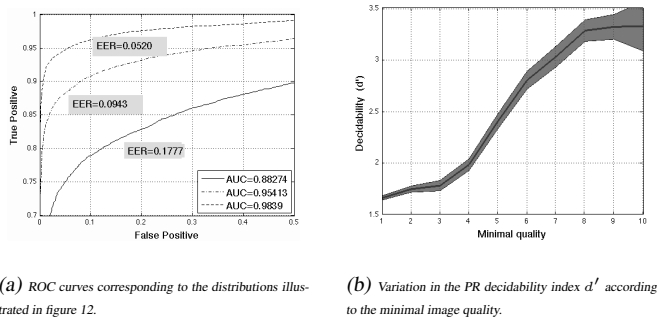
Fig. 13. Improvements in recognition performance due to quality assessment.

The experiments about the occlusions and area factors (figure 14c) enabled us to conclude that effectiveness is directly correlated to the available area of the iris. This can be observed just up to a limit (around the 6th quality bean), above which effectiveness did not consistently improved. Also, the higher decidability observed for bigger irises may be related to the fact that images of UBIRIS.v2 that were acquired at close distances tend to have proportionally less proportion of occluded iris, due to the specific lighting conditions of the environment.

(a) Degradation in recognition effectiveness due to focus and motion blur.

(b) Degradation in recognition effectiveness due to off-angle and pupillary dilations.

(c) Degradation in recognition effectiveness due to the available area and iris occlusions.

(d) Degradation in recognition effectiveness due to the levels of iris pigmentation.
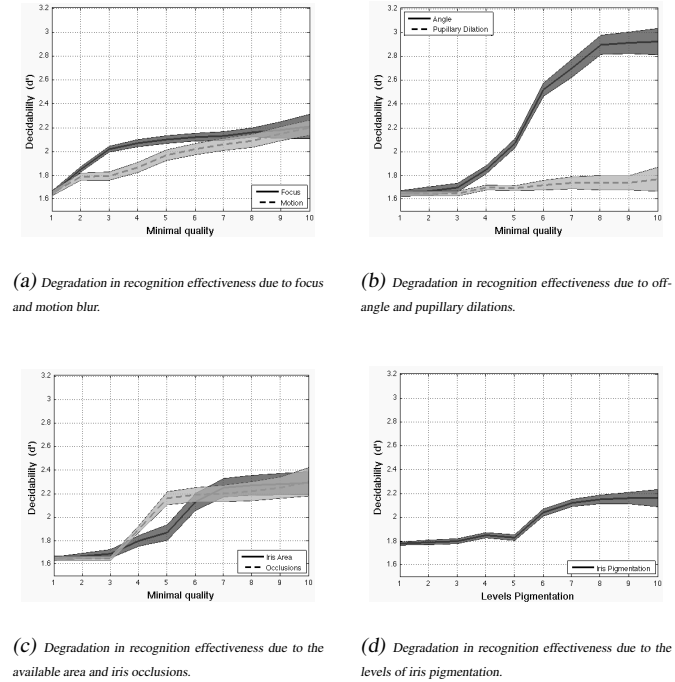
Fig. 14. Degradation in recognition effectiveness due to each of the quality factors assessed in this paper. Line plots relate the decidability index d' to the minimal quantized and normalized quality scores α^* of the used samples. The gray regions denote 95% confidence intervals.

previously published works (e.g., [19]). We suspect that this was mainly due to the spectrum of light of our data sets: in opposition to NIR data, the pupillary boundary of VW images is much more difficult to segment than the scleric. For such, significant inaccuracies in the segmentation of the pupil might have occurred and corrupted the pupillary dilation experiments. Figure 14d confirms that the levels of iris pigmentation constitute an obstacle to VW iris recognition, as the decidability values obtained for light pigmented irises (rightmost data points, mostly blue and light green irises) were notoriously higher than those obtained when heavily pigmented images were also used. One probable reason for this is the spectral absorbance of the predominant pigment of the human iris (brown-black Eumelanin), that has a peak in the VW and turns the discriminating patterns of heavily pigmented irises (ridges, valleys, furrows and crypts) more difficult to capture.

Finally, we tested the independence between the generated quality scores. Table II gives the Pearson's sample correlation coefficient r for each pair of quality scores (α_1, α_2), obtained for the UBIRIS.v2 data set:

$$r = \frac{\sum_{i=1}^{n} \left(\alpha_1(i) - \overline{\alpha_1} \right) \left(\alpha_2(i) - \overline{\alpha_2} \right)}{\left(\sum_{i=1}^{n} \left(\alpha_1(i) - \overline{\alpha_1} \right)^2 \right)^{0.5} \left(\sum_{i=1}^{n} \left(\alpha_2(i) - \overline{\alpha_2} \right)^2 \right)^{0.5}}$$

(22)

where $\alpha(i)$ gives the quality score of sample i and $\overline{\alpha}$ its mean value. Moderate to significant correlation was observed between the (focus, motion), (off-angle, occlusions), (off-angle, area), (occlusions, pupillary dilation) and (area, pupillary dilations) scores. With exception to the former, all the remaining have evident biological roots, which contributes for the successful empirical evaluation of the proposed iris quality assessments.

	α_f	α_m	α_a	α_o	α_p	α_c	α_d
α_f	$-$	$-$	$-$	$-$	$-$	$-$	$-$
α_m	-0.27	$-$	$-$	$-$	$-$	$-$	$-$
α_a	-0.02	0.10	$-$	$-$	$-$	$-$	$-$
α_o	-0.01	0.06	0.37	$-$	$-$	$-$	$-$
α_p	-0.14	0.04	0.00	0.00	$-$	$-$	$-$
α_c	0.00	0.01	-0.29	-0.03	0.00	$-$	$-$
α_d	0.00	0.00	0.01	-0.24	0.16	-0.39	$-$

D. Adaptability to Near Infra-Red Images

Even considering that the proposed method was devised to handle VW data, it might be useful to discuss its adaptability to NIR data that corresponds to the currently used in the commercially deployed systems. For such, we adopted a parameterized segmentation method composed by an elliptical integro-differential operator [38] that gives the coordinates of the limbic and pupillary boundaries, and then used active contours based on Fourier series (with 17 and 4 coefficients for pupillary and limbic boundaries) for fine representation [10]. Specular reflections were detected by means of hard thresholds and eyelashes by modal analysis of the intensities histograms within the iris. Then, based in the NIR sample and its segmentation mask, all the subsequent phases of the proposed method perform similarly (as overviewed in figure 2), with exception to the iris pigmentation assessment that becomes meaningless. Also, it should be emphasized that some of the quality assessments outputs have different ranges of the illustrated in figure 10 and new reference values have to be obtained. Figure 15 illustrates two quality assessments for images of the CASIA.v3 (Lamp) and WVU iris databases. Not surprisingly, the observed pupillary dilation scores were significantly lower than the typically obtained in VW data (pupils more dilated), which led us to suspect that there were reduced amounts of visible light in the acquisition scenes of such NIR data sets. Further, the improvements in performance observed when using exclusively the most interior parts of the iris in focus assessment were confirmed. Also, the phases described in sections III-D and III-E, that perform with lower computational cost when comparing to the work described in [22], appear to produce plausible results in NIR data too.

V. CONCLUSIONS

Due to potential forensic applications, the possibility of performing iris recognition in uncontrolled lighting conditions and at larger distances motivates growing research efforts. Here, quality assessment is a key issue, due to the factors that typically degrade the quality of data acquired in such acquisition setup. Most of the published approaches to assess iris image quality were devised to deal with NIR *controlled* data and do not appropriately handle the the specificity of *real-world VW* data. This motivated the proposal of an automated method to assess the quality of such data, in terms of the factors that are known to be correlated with biometric effectiveness: focus, motion, angle, occlusions, area, pupillary
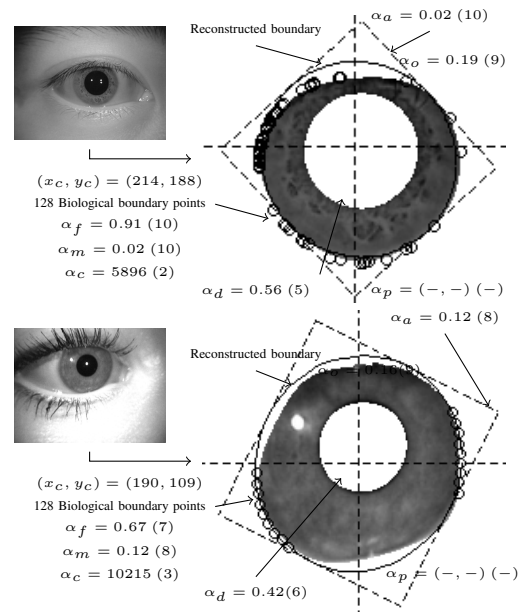
Fig. 15. Examples of the application of the proposed iris quality assessments to NIR images of the CASIA.v3 Lamp (left column) and of the WVU (right column) databases.

dilation and levels of iris pigmentation. The proposed quality assessment strategy starts by the estimation of the center of the iris and of its deemed biological boundaries. These are used to assess each quality factor and generate a numeric value that — empirically — was observed to be in agreement with the human visual notion of *quality*. Also, we reported consistent improvements in performance due to data quality assessment, when the poorest quality samples were not considered for the recognition process.

ACKNOWLEDGEMENTS

REFERENCES

[1] A. Abhyankar and S. Schuckers. Iris quality assessment and bi-orthogonal wavelet base dencoding for recognition. *Pattern Recognition, vol. 42*, pages 1878–1894, 2009.

[2] American National Standards Institute. American national standard for the safe use of lasers and LEDs used in optical fiber transmission systems (ANSI Z136.2), 1988.

[3] E. Arvacheh and H. Tizhoosh. *A study on Segmentation and Normalization for Iris Recognition*. Msc. dissertation, University of Waterloo, 2006.

[4] A. Basit and M. Y. Javed. Iris localization via intensity gradient and recognition through bit planes. In *Proceedings of the International Conference on Machine Vision (ICMV 2007)*, pages 23–28, December 2007.

[5] K. Bowyer, K. Hollingsworth, and P. Flynn. Image understanding for iris biometrics: A survey. *Computer Vision and Image Understanding, vol. 110, no. 2*, pages 281–307, 2008.

[6] Y. Chen, S. C.. Dass and A. K. Jain. Localized iris image quality using 2-D wavelets. In *Proceedings of the International Conference on Biometrics*, pages 373–381, 2006.

[7] Commission International de l'Eclarirage. Photobiological safety standards for safety standards for lamps,. Report of TC 6-38; (CIE 134-3-99), 1999.

[8] J. G. Daugman. Biometric Decision Landscapes. Tech Report TR482, http://www.cl.cam.ac.uk/users/jgd1000/biomdecis.ps, 2000.

[9] J. G. Daugman. How Iris Recognition Works. *IEEE Transactions on Circuits, Systems and Video Technology, vol. 14, issue 1*, pages 21–30, 2004.

[10] J. G. Daugman. New methods in iris recognition. *IEEE Transactions on Systems, Man, and Cybernetics - Part B: Cybernetics, vol. 37, no. 5*, pages 1167–1175, 2007.

[11] J. G. Daugman and C. Downing. Effect of Severe Image Compression on Iris Recognition Performance. *IEEE Transactions on Information Forensic and Security, vol. 3, no. 1*, pages 52–61, 2008.

[12] M. Dobes, J. Martineka, D. S. Z. Dobes, and J. Pospisil. Human eye localization using the modified hough transform. *Optik, vol. 117*, pages 468–473, 2006.

[13] V. Dorairaj, N. Schmid and G. Fahmy. Performance evaluation of non-ideal iris based recognition system implementing global ICA encoding. In *Proceedings of the International Conference on Image Processing, vol. 3*, pages 285–288, 2005.

[14] F. Imai. Preliminary experiment for spectral reflectance estimation of human iris using a digital camera. Technical report, Munsell Color Science Laboratories, Rochester Institute of Technology, 2000.

[15] K. Grabowski, W. Sankowski, M. Zubert and N. Napieralska. Focus Assessment Issues in Iris Image Acquisition System. In *proceedings of the 14th International Conference MIXDES 2007*, pages 628–631, 2007.

[16] G. Toussaint. Solving geometric problems with the rotating calipers . In *proceedings of the IEEE MELECON'83*, Athens, Greece, May 1983.

[17] Z. He, T. Tan, Z. Sun and X. Qiu. Robust eyelid, eyelash and shadow localization for iris recognition. In *Proceedings of the International Conference on Image Processing*, pages 265–268, 2009.

[18] Z. He, T. Tan, Z. Sun and X. Qiu. Towards Accurate and Fast Iris Segmentation for Iris Biometrics. *IEEE Transactions on Pattern Analysis and Machine Intelligence , vol. 31, no. 9*, pages 1670–1684, 2009.

[19] K. P. Hollingsworth, K. W. Bowyer and P. J. Flynn. The Importance of small pupils: a study of how pupil dilation affects iris biometrics. In *Proceedings of the International Conference on Biometrics*, pages 1–6, 2008.

[20] J. Jang, K. R. Park, J. Kim and Y. Lee. New focus assessment method for iris recognition systems. *Pattern Recognition Letters*, vol. 29, no. 13, pages 1759-1767, 2008.

[21] J. R. Matey, D. Ackerman, J. Bergen, and M. Tinker. Iris recognition in less constrained environments. In *Springer Advances in Biometrics: Sensors, Algorithms and Systems*, pages 107–131, October 2007.

[22] N. Kalka, J. Zuo, N. Schmid and B. Cukic. Estimating and Fusing Quality Factors for Iris Biometric. *IEEE Transactions on Systems, Man and Cybernetics, Part A*, vol. 40, no. 3, pages 509–524, 2010.

[23] B. J. Kang and K. R. Park. A study on iris image restoration. In *Proceedings of the International Conference on Audio- and Video-Based Biometric Person Authentication*, pages 31–40, 2005.

[24] B. J. Kang and K. R. Park. A Robust eyelash detection based on iris focus assessment. *Pattern Recognition Letters, vol. 28, no. 13*, pages 1630–1639, 2007.

[25] B. J. Kang and K. R. Park. A new multi-unit iris authentication based on quality assessment and score level fusion for mobile phones. *Machine Vision and Applications, DOI: 10.1007/s00138-009-0184-0*, 2009.

[26] E. Krichen, S. Garcia-Salicetti and B Dorizzi. A new probabilistic iris quality measure for comprehensive noise detection. In *Proceedings of the IEEE International Conference on Biometrics: Theory, Applications, and Systems*, pages, 1–6, 2007.

[27] X. Liu, K. W. Bowyer, and P. J. Flynn. Experiments with an improved iris segmentation algorithm. In *Proceedings of the Fourth IEEE Workshop on Automatic Identification Advanced Technologies*, pages 118–123, October 2005.

[28] G. Lu, J. Qi and Q. Liao. A New Scheme of Iris Image Quality Assessment. In *Proceedings of the Third International Conference on International Information Hiding and Multimedia Signal Processing, vol. 1*, pages 147–150, 2007.

[29] P. Meredith and T. Sarna. The phisical and chemical properties of eumelanin. *Pigment Cell Research, vol. 19*, pages 572–594, 2006.

[30] K. Nandakumar, Y. Chen, A. K. Jain and S. Dass. Quality based score level fusion in multibiometric systems. In *Proceedings of the International Conference on Pattern Recognition*, pages 473–476, 2006.

[31] H. Proença and L. A. Alexandre. A method for the identification of noisy regions in normalized iris images. In *Proceedings of the International Conference on Pattern Recognition, vol. 4*, pages 405–408, 2006.

[32] H. Proença, S. Filipe, R. Santos, J. Oliveira and L. A. Alexandre The UBIRIS.v2: A Database of Visible Wavelength Iris Images Captured On-The-Move and At-A-Distance. *IEEE Transactions on Pattern Analysis and Machine Intelligence*, vol. 32, no. 8, pages 1502–1516, 2010.

[33] H. Proença. Iris Recognition: On the Segmentation of Degraded Images Acquired in the Visible Wavelength. *IEEE Transactions on Pattern Analysis and Machine Intelligence*, vol. 32, no. 8, pages 1529–1535, 2010.

[34] H. Proença. On the Feasibility of the Visible Wavelength, At-A-Distance and On-The-Move Iris Recognition. In *Proceedings of the IEEE Symposium Series on Computational Intelligence in Biometrics: Theory, Algorithms, and Applications*, vol. 1, pages 9–15, 2009.

[35] H. Proença and L. A. Alexandre. Introduction to the Special Issue on the Segmentation of Visible Wavelength Iris Images Captured At-a-distance and On-the-move. *Image and Vision Computing*, vol. 28, no. 2, pages 213–213, 2010.

[36] A. Ross, S. Crihalmeanu, L. Hornak, and S. Schuckers. A centralized web-enabled multimodal biometric database. In *Proceedings of the 2004 Biometric Consortium Conference (BCC)*, U.S.A, 2004.

[37] A. Ross and S. Shah. Iris segmentation using geodesic active contours. *IEEE Transactions on Information Forensics and Security, Special issue on electronic voting*, vol. 4, issue 4, pages 824–836, U.S.A, 2009.

[38] S. Schuckers, N. Schmid, A.Abhyankar, V. Dorairaj, C. Boyce, and L. Hornak. On techniques for angle compensation in nonideal iris recognition. *IEEE Transactions on Systems, Man and Cybernetics-Part B: Cybernetics, vol. 37, no. 5*, pages 1176–1190, October 2007.

[39] M. Tico and P. Kuosmanen. Weighted least squares method for the approximation of directional derivatives. In *Proceedings of the IEEE International Conference on Acoustics, Speech, and Signal Processing*, vol. 3, pages 1681–1684, U.S.A, 2001.

[40] M. Dobes and L. Machala. UPOL Iris Database. *http://phoenix.inf.upol.cz/iris/*, U.S.A, 2004.

[41] M. Vatsa, R. Singh, and A. Noore. Improving iris recognition performance using segmentation, quality enhancement, match score fusion, and indexing. *IEEE Transactions on Systems, Mans and Cybernetics - B, vol. 38, no. 4*, pages 1021–1035, 2008.

[42] J. Wan, X. He and P. Shi. An Iris Image Quality Assessment Method Based on Laplacian of Gausian Operation. In *Proceedings of the IAPR IAPR Conference on Machine Vision Applications*, pages 248–251, 2007.

[43] Z. Wei, T. Tan, Z. Sun and J. Cui. Robust and Fast Assessment of Iris Image Quality. In *Proceedings of the International Conference on Biometrics*, pages 464–471, 2006.

[44] X. Ye, P. Yao, F. Long, Z. Zhuang. Iris image realtime pre-estimation using compound neural network. In *Proceedings of the International Conference on Biometrics*, pages 450–456, 2006.

[45] G. Zhang and M. Salganicoff. Method of measuring the focus of close-up image of eyes. U.S. Patent No. 5,953,440,, 1999.

[46] T. Tan, Z. He, and Z. Sun. Efficient and robust segmentation of noisy iris images for non-cooperative segmentation. *Elsevier Image and Vision Computing Journal, Special Issue on the Segmentation of Visible Wavelength Iris Images, vol. 22, no. 2*, pages 223–230, 2010.

[47] C.T. Zahn and R.Z. Roskies. Fourier Descriptors for Plane Closed Curves. *IEEE Transactions on Computers, vol. 21, no. 3*, pages 269–281, 1972.

[48] J. Zuo and N. Schmid. An automatic algorithm for evaluating the precision of iris segmentation. In *Proceedings of the IEEE Conference on Biometrics: Theory, Applications and Systems*, pages 1–6, 2008.

[49] J. Zuo and N. Schmid. Global and local quality measures for NIR iris video. In *Proceedings of the International Conference On Computer Vision and Pattern Recognition*, pages 120–125, 2009.